

# Flexible and Stackable Laser-Induced Graphene Supercapacitors

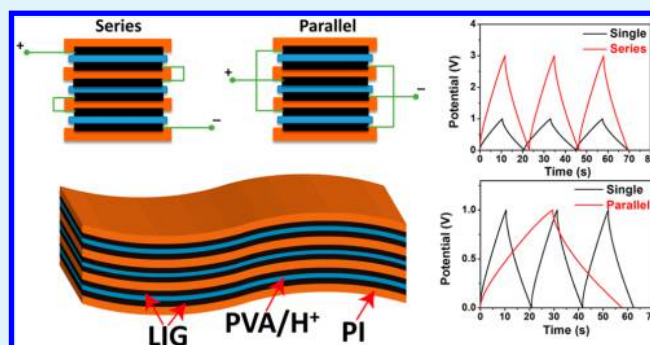
Zhiwei Peng,<sup>†,‡</sup> Jian Lin,<sup>‡,§,‡</sup> Ruquan Ye,<sup>†</sup> Errol L. G. Samuel,<sup>†</sup> and James M. Tour<sup>\*,†,§,‡</sup>

<sup>†</sup>Department of Chemistry, <sup>‡</sup>Smalley Institute for Nanoscale Science and Technology, and <sup>§</sup>Department of Materials Science and NanoEngineering, Rice University, 6100 Main Street, Houston, Texas 77005, United States

## Supporting Information

**ABSTRACT:** In this paper, we demonstrate that by simple laser induction, commercial polyimide films can be readily transformed into porous graphene for the fabrication of flexible, solid-state supercapacitors. Two different solid-state electrolyte supercapacitors are described, namely vertically stacked graphene supercapacitors and in-plane graphene microsupercapacitors, each with enhanced electrochemical performance, cyclability, and flexibility. Devices with a solid-state polymeric electrolyte exhibit areal capacitance of  $>9 \text{ mF/cm}^2$  at a current density of  $0.02 \text{ mA/cm}^2$ , more than twice that of conventional aqueous electrolytes. Moreover, laser induction on both sides of polyimide sheets enables the fabrication of vertically stacked supercapacitors to multiply its electrochemical performance while preserving device flexibility.

**KEYWORDS:** scalable, laser, graphene, supercapacitor, flexible, stacking, solid-state



Though the past decade has witnessed rapid growth in the study of batteries and supercapacitors (SCs),<sup>1–7</sup> two topics still remain as primary challenges in the development of advanced energy storage devices. The first challenge is in the fabrication of a single device that combines the high power performance of SCs with the high energy density of batteries.<sup>8,9</sup> The second challenge involves miniaturizing energy-storage units to meet the size limitations of portable, microelectronic systems.<sup>10–13</sup> To address the first issue, an active electrode material with highly accessible surface area and conductivity is desired in order to form a more stable electrochemical double layer (EDL) with fast ionic transport.<sup>14,15</sup> Also, compact stacking of individual SCs with minimal contact resistance can multiply the operational voltage or energy storage while maintaining good electrochemical behavior and further increase the power or energy density.<sup>16–19</sup> As for the second challenge, microsupercapacitors (MSCs) are sought with an in-plane structure that would be suitable for use in microscale integrated circuits.<sup>6,20</sup> However, most fabrication methods require conventional lithographic techniques for device patterning,<sup>21</sup> which are costly when the devices are considered for low-cost consumer applications.

Because of their exceptional physical and chemical properties, graphene-based materials have shown great potential for use in next-generation flexible and portable energy-storage microdevices, but their commercialization has been impeded because of the relatively high-cost or complex synthetic routes associated with the synthesis of graphene.<sup>22–25</sup> For example, a recently developed method to make graphene uses laser scribing of graphene oxide (GO) films, where GO is then reduced,<sup>26–28</sup> patterned, and fabricated to make graphene-based devices that exhibit remarkable electrochemical perform-

ance. Unfortunately, the synthesis of GO and its subsequent formation into films is still far from commercialization in bulk quantities.<sup>29,30</sup> Furthermore, recent studies have shown that GO decomposes over time, which can lead to significant current leakage or device changes within GO-derived devices.<sup>31</sup>

Our group recently showed a simple, scalable method to rapidly make laser-induced graphene (LIG) and fabricate microsupercapacitors (MSCs) using laser induction of commercial polyimide (PI) sheets.<sup>32</sup> By this approach, the polymeric sheet is chemically transformed by laser absorption into a porous graphene structure with rich ultrapolycrystalline domains of pentagon-heptagon rings. Here, we extend this method to fabricate flexible LIG based SCs by using a solid-state polymeric electrolyte, poly(vinyl alcohol) (PVA) in  $\text{H}_2\text{SO}_4$ . Two flexible, solid-state SCs are described: LIG-SCs and LIG-MSCs. These devices show areal capacitance of  $>9 \text{ mF/cm}^2$  at a discharge current density of  $0.02 \text{ mA/cm}^2$ , which is over twice that achieved when using aqueous electrolytes.<sup>32</sup> Furthermore, by laser induction of both sides of the PI sheets, solid-state LIG-SCs can be stacked to form high-density energy storage devices that multiply their electrochemical performance while maintaining flexibility.

## RESULTS AND DISCUSSION

Figure 1a schematically illustrates the process in fabricating flexible, solid-state LIG-SCs. The process begins by first transforming the surface of a PI sheet into porous graphene

Received: December 23, 2014

Accepted: January 13, 2015

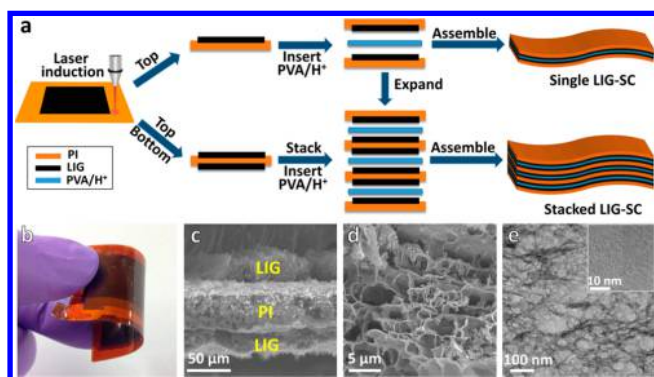


**Figure 1.** Fabrication and characterization of LIG-SCs. (a) Schematic illustration showing the fabrication process for assembling a single LIG-SC and stacked LIG-SC. (b) Optical image of a fully assembled single LIG-SC manually bent. (c) Cross-sectional SEM image of a PI substrate with both sides laser-induced to form graphene. (d) SEM image of the LIG films showing a porous 3D network. (e) TEM image of a LIG thin film showing nanosized wrinkles and ripples. Inset is a HRTEM image of a LIG nanosheet showing numerous graphene edges.

under laser induction using a commercially available, computer controlled CO<sub>2</sub> laser cutting system, and then assembling either a single LIG-SC or stacked LIG-SC. Figure S1 in the Supporting Information and Figure 1b show the photograph of a half-side LIG electrode and a typical single LIG-SC device manually bent to demonstrate its intrinsic flexibility. A critical advantage of this fabrication method is that LIG can be easily produced under ambient conditions on both sides of the PI sheet with a remaining central insulating PI layer to separate them (Figure 1c), which then facilitates layer-by-layer stacking of LIG-SCs. Alternatively, this same technique can also be used to pattern LIG into interdigitated electrodes for fabrication of solid state in-plane LIG-MSCs (see Figure S2 in the Supporting Information). This one-step approach is both straightforward and cost-effective, and could easily fit into a scalable, roll-to-roll process for industrial production of graphene-based energy storage systems.

The formed LIG showed very similar morphology and graphene properties to our previous report.<sup>32</sup> Figure 1c shows a cross-sectional scanning electron microscope (SEM) image, where a thick LIG layer ( $\sim 25\ \mu\text{m}$ ) is clearly formed on both sides of the PI substrate after laser induction and is separated by an unexposed middle PI layer that serves to electrically isolate the top and bottom LIG layers from each other. The SEM image in Figure 1d shows the porous structure of LIG and the transmission electron microscope (TEM) image in Figure 1e shows the nanoscale ripples and wrinkles in the LIG films. Also, the high-resolution TEM (HRTEM) image in the inset of Figure 1e reveals that these LIG sheets contain numerous graphene edges resulting in more accessible surface area and therefore better electrochemical performance. The Raman spectrum of LIG in Figure S3a in the Supporting Information clearly shows three characteristic peaks of graphene derived material, specifically, a D peak at  $\sim 1350\ \text{cm}^{-1}$  induced by defects, folding or symmetry-broken carbon, G peak at  $\sim 1590\ \text{cm}^{-1}$  generated by graphitic carbon, and a 2D peak at  $\sim 2700\ \text{cm}^{-1}$  originating from second-order zone boundary phonons.<sup>33,34</sup> Note that the D peak could arise from numerous graphene edges existing in LIG flakes, which are also observed in the above TEM images.<sup>35,36</sup> The XRD pattern in Figure S3b

shows a prominent peak at  $2\theta = 25.6^\circ$ , indicative of an interlayer spacing of  $\sim 3.4\ \text{\AA}$  between (002) graphitic crystal planes in LIG. The high degree of graphitization of LIG is further supported by thermogravimetric analysis (TGA) under argon (see Figure S4 in the Supporting Information), because PI decomposes at  $\sim 550\ ^\circ\text{C}$ , whereas LIG remains stable at  $>900\ ^\circ\text{C}$ . BET analysis in Figure S5a in the Supporting Information shows that the surface area of LIG is  $\sim 330\ \text{m}^2/\text{g}$  with a pore size distribution between 2 and 10 nm (see Figure S5b in the Supporting Information).

To investigate its electrochemical performance, we first fabricated LIG into a flexible, single LIG-SC by sandwiching a solid, polymeric electrolyte (PVA and H<sub>2</sub>SO<sub>4</sub>) between two single-sided LIG-PI sheets, which functioned both as the working electrode and current collector. The cyclic voltammetry (CV) curves shown in Figure 2a were pseudorectangular

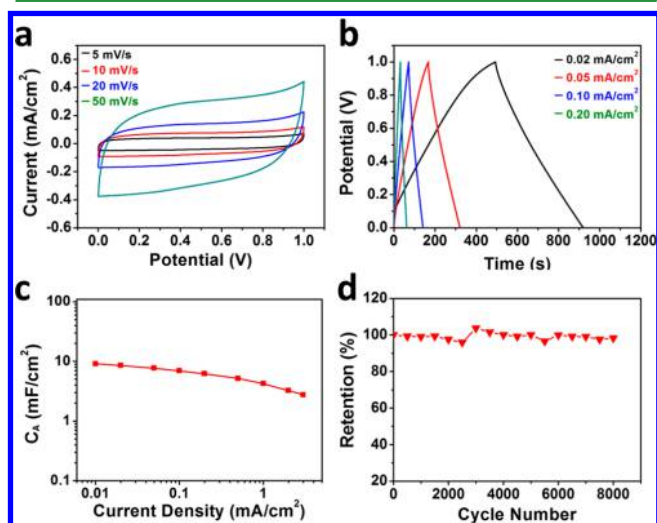


**Figure 2.** Electrochemical performance of a single LIG-SC. (a) CV curves of LIG-SCs at scan rates of 5, 10, 20, and 50 mV/s. (b) Galvanostatic CC curves of LIG-SCs at current densities of 0.02, 0.05, 0.10, and 0.20 mA/cm<sup>2</sup>. (c) Specific areal capacitances calculated from CC curves as a function of current density. (d) Cyclability testing of LIG-SCs with a CC current density of 0.8 mA/cm<sup>2</sup>.

over varying scan rates (5, 10, 20, and 50 mV/s), which is indicative of good EDL stability. In addition, Figure 2b shows that when different current densities (0.02, 0.05, 0.10, and 0.20 mA/cm<sup>2</sup>) were applied, the galvanostatic charge–discharge (CC) curves were nearly triangular, indicating good capacitive behavior. From the initial stage of discharge, the negligible voltage drop shows that the device has low internal resistance. Additional CV curves at higher scan rates and CC curves at higher current densities can be found in Figure S6 in the Supporting Information to show that LIG-SC can be charged and discharged over a wide range of scan rates (5 to 1000 mV/s) and current densities (0.02 to 2.0 mA/cm<sup>2</sup>). The calculated areal capacitances ( $C_A$ ) from the CC curves with its corresponding current densities are shown in Figure 2c, with the highest capacitance being 9.11 mF/cm<sup>2</sup> at a corresponding current density of 0.01 mA/cm<sup>2</sup>, comparable to the values reported in the literature for graphene based microsupercapacitors (0.4 to 2 mF/cm<sup>2</sup>).<sup>6,27</sup> Also, the single LIG-SC shows excellent cycle stability, where after 8000 CC cycles, the device retained more than 98% of its capacity (Figure 2d).

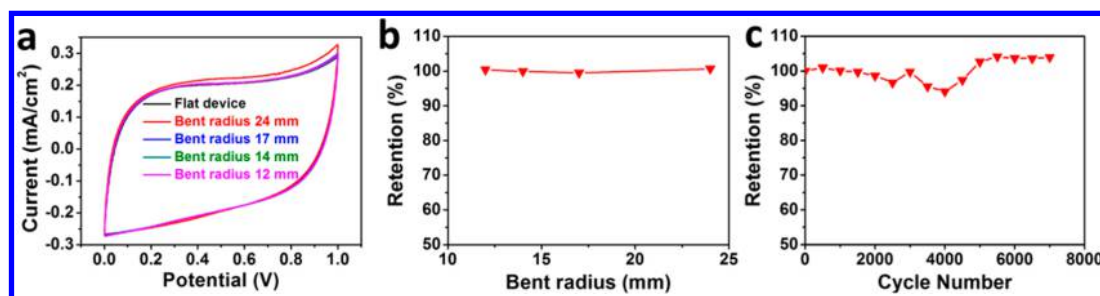


**Figure 3.** Electrochemical performance of LIG-SCs under bending. (a) CV curves of LIG-SC at varying bending radii. The scan rate was 0.02 V/s. (b) Capacity retention at different bending radius. Capacitance retention was calculated from CC curves at a current density of 0.05 mA/cm<sup>2</sup>. (c) Cyclability testing of flexible LIG-SCs. Capacitance retention was calculated from CC curves at a current density of 0.4 mA/cm<sup>2</sup>.

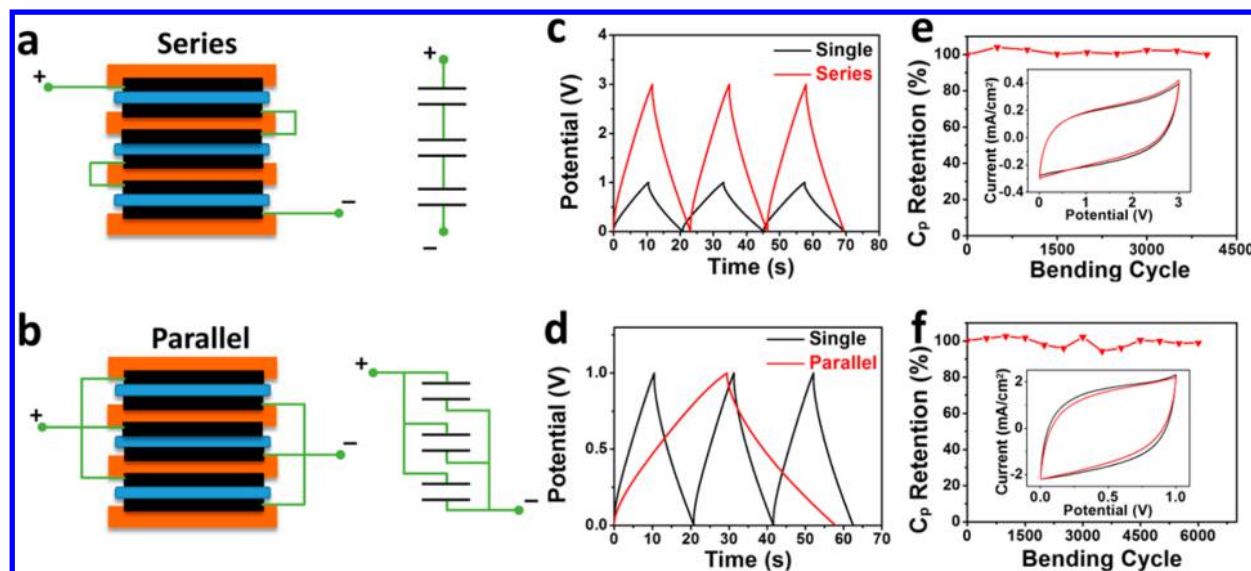


**Figure 4.** Electrochemical performances of stacked LIG-SCs in series and parallel circuits. (a) Illustration of a stacked series LIG-SC and its corresponding circuit diagram. (b) Illustration of a stacked parallel LIG-SC and its corresponding circuit diagram. (c) Galvanostatic CC curves comparing a single LIG-SC to a stacked series LIG-SC at a current density of 0.5 mA/cm<sup>2</sup>. (d) Galvanostatic CC curves comparing a single LIG-SC to a stacked parallel LIG-SC at a current density of 0.5 mA/cm<sup>2</sup>. (e) Cyclability testing of a flexible stacked series LIG-SC at a current density of 0.5 mA/cm<sup>2</sup>. Inset shows the initial CV curves (black) and the 4000th CV curve (red) at a scan rate of 0.1 V/s. (f) Cyclability testing of a flexible, stacked parallel LIG-SC at a current density of 1.0 mA/cm<sup>2</sup>. Inset shows the initial CV curves (black) and the 6000th CV curve (red) at a scan rate of 0.1 V/s.

Next, the assembled single LIG-SCs performance stability was tested under mechanical bending. Figure 3a compares the CV curves of a flexible single LIG-SC over different bending radii (12 mm to 24 mm) and remarkably shows that the bent device exhibits nearly identical behavior to the flat LIG-SC. Also, Figure 3b shows that the calculated  $C_A$  under different bending radii remained almost constant. From Figure 3c, the  $C_A$  was well-maintained after 7000 bending cycles at a radius of 14 mm, indicating that repeated bending has little effect on its electrochemical performance. These findings further reinforce the assertion that LIG-SC is a promising candidate for energy storage devices in flexible, portable, and wearable electronics.

An additional advantage of this method is the capability of forming LIG on both sides of an individual PI sheet thus enabling the fabrication of stacked LIG-SC (Figure 1). Panels a and b in Figure 4 are illustrations of a series and parallel LIG-SC assembled from stacked solid-state LIG-SCs, where double-sided LIG sheets are layered with alternating deposits of polymeric electrolyte and capped with single-sided LIG-PI sheets. Panels c and d in Figure 4 show the CC curves of a 3-stack solid-state series and parallel LIG-SC, respectively. Compared to a single LIG-SC, the stacked series LIG-SC has

a 2× higher working voltage window, whereas the stacked parallel LIG-SC shows a 2× longer discharge time when operated at the same current density, resulting in a 2x higher capacitance. In both configurations, the CC curves present nearly triangular shapes with miniscule voltage drop indicating negligible internal and contact resistances. Additional CV and CC curves at various scan rates and current densities for the stacked series and parallel LIG-SCs are shown in Figure S7 and S8 in the Supporting Information to demonstrate their remarkable durability over a wide range of scan rates and current densities. Even though the SCs are stacked, the assembled stacked LIG-SCs still show high flexibility. Panels e and f in Figure 4 shows that the capacitance of the stacked LIG-SC circuits are nearly 100% of their initial value even after being subjected to several thousand bending cycles at a bending radius of 17 mm. Additionally, the CV curves at different bending cycles are nearly overlapped (Figure 4e, f insets), indicating well-maintained flexibility.

The laser induction process can also be used to synthesize and pattern LIG into interdigitated electrodes for the fabrication of in-plane LIG-MSCs (see Figure S2 in the Supporting Information). Figure 5a is an illustration of a



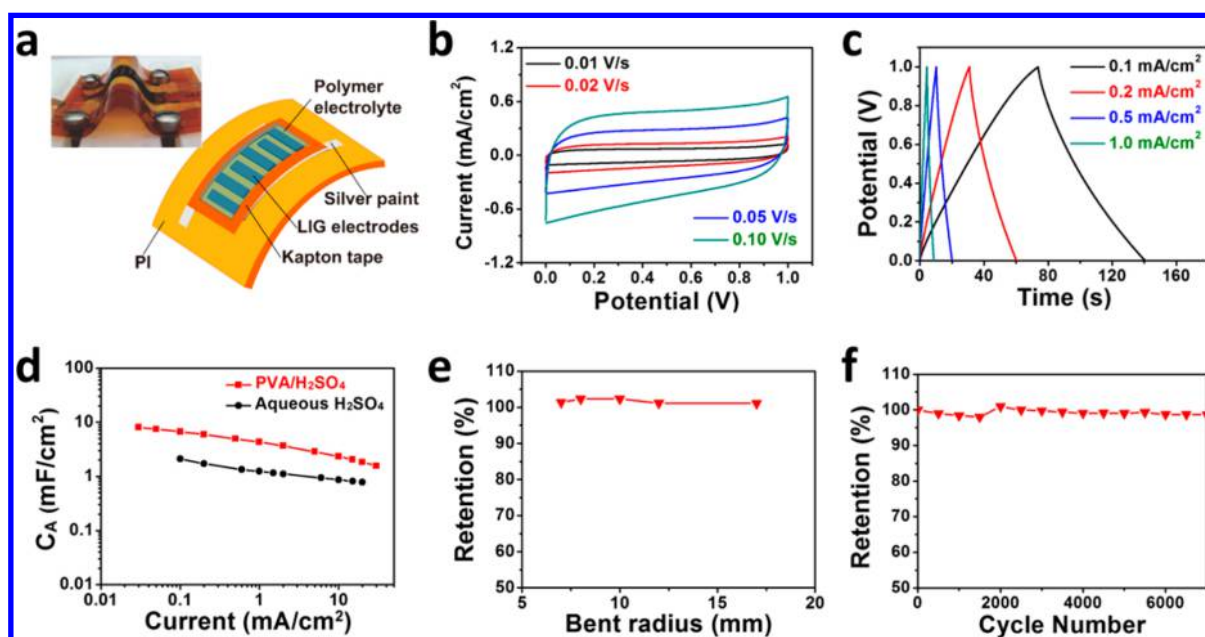


**Figure 5.** Electrochemical performances of LIG-MSC devices. (a) Illustration of a flexible LIG-MSC. Inset is a photograph of a LIG-MSC fixed at a bending radius of 12 mm. (b) CV curves of LIG-MSCs at scan rates of 10, 20, 50, and 100 mV/s. (c) Galvanostatic CC curves of LIG-MSCs at current densities of 0.1, 0.2, 0.5, and 1.0 mA/cm². (d) Specific  $C_A$  of LIG-MSCs from aqueous 1 M H<sub>2</sub>SO<sub>4</sub> and PVA/H<sub>2</sub>SO<sub>4</sub> calculated from CC curves as a function of the current density. (e) Capacity retention of LIG-MSC at different bending radii. Capacitance retention was calculated from CC curves at a current density of 0.5 mA/cm². (f) Cyclability testing of flexible LIG-MSCs. Capacitance retention was calculated from CC curves at a current density of 0.5 mA/cm².

flexible LIG-MSC fabricated on a PI sheet that uses PVA/H<sub>2</sub>SO<sub>4</sub> as solid-state electrolyte. Figure 5b shows CV curves of the LIG-MSC device at different scan rates (0.01, 0.02, 0.05, and 0.1 V/s) with stable pseudorectangular shape due to good EDL formation. Figure 5c shows the galvanostatic CC curves of LIG-MSCs at different current densities (0.1, 0.2, 0.5, and 1.0 mA/cm²), all of which are nearly triangular due to their excellent capacitive behaviors. Figure S9 in the Supporting Information shows additional CV curves at higher scan rates and CC curves at higher current densities. The calculated  $C_A$  from CC curves at different current densities are plotted in Figure 5d, where the devices strikingly exhibit a capacitance of greater than 9 mF/cm² at a current density of 0.02 mA/cm². Interestingly, at the same current densities the capacitances of the solid-state LIG-MSCs are twice that of aqueous H<sub>2</sub>SO<sub>4</sub> electrolyte LIG-MSCs.<sup>32</sup> This improvement could come from the high hydrophobicity of the LIG material and better interface formation between LIG electrodes and the organic polymer electrolyte. Furthermore, capacitance of the solid-state LIG-MSCs remains over 1.9 mF/cm² even when operated at a higher current density of 30 mA/cm², indicating high power performance of the device. Electrochemical impedance measurements (see Figure S10 in the Supporting Information) further supports faster ionic transport and better electrode–electrolyte interface in LIG-MSCs using PVA/H<sub>2</sub>SO<sub>4</sub> as the electrolyte. The near absence of the semicircle in the case of MSCs with PVA/H<sup>+</sup> implies that there is high ionic conductivity at the interface of the LIG electrode and polymer electrolyte. Also, the higher slope in the Nyquist plot for MSCs with PVA/H<sup>+</sup> indicates that they have more capacitive behavior. The cyclability of solid-state LIG-MSCs was also tested over 8000 CC cycles with <10% capacitance degradation (see Figure S11 in the Supporting Information). To test their circuit performance, we connected two single LIG-MSC devices

in either series or parallel configurations as shown in Figure S12 in the Supporting Information. As expected, the working voltage was doubled when LIG-MSCs were in series, while the discharge runtime increased nearly 100% when LIG-MSCs were in parallel. In both cases, because of the solid-state electrolyte, the CC curves maintained their triangular shape and the LIG-MSC showed outstanding flexibility (Figure 5a inset). Figure 5e shows that the in-plane LIG-MSCs made from LIG exhibits nearly 100% of its calculated capacitance regardless of bending radii. Similar to the single LIG-SC, CV curves of LIG-MSC over different bending radii are almost identical to the ones in the flat devices (see Figure S13 in the Supporting Information). After 7000 bending cycles, the capacitance remained at its initial value (Figure 5f), further supporting the universality of this laser induction method in producing energy storage units.

Finally, Figure 6 is a Ragone plot comparing single LIG-SCs and LIG-MSCs in either aqueous or solid-state polymeric electrolytes to commercially available electrolytic capacitors and Li thin film batteries.<sup>10,26,27</sup> Although aluminum (Al) electrolytic capacitors deliver ultrahigh power, their energy density is 2 orders of magnitude lower than LIG-derived devices. Similarly, although lithium-ion thin-film batteries can provide high energy density, their power performance is 3 orders of magnitude lower than either single LIG-SCs or LIG-MSCs. Interestingly, when compared to LIG-MSC using 1 M aqueous H<sub>2</sub>SO<sub>4</sub> as the electrolyte, LIG-MSC with a solid-state polymer electrolyte stores ~2× more energy. Also, a comparison between single LIG-SCs and LIG-MSCs shows that LIG-MSCs have a higher power density than LIG-SC, likely because of the reduced ion diffusion length between the microelectrodes in the LIG-MSC device. Ragone plots of single LIG-SCs and LIG-MSCs with specific areal energy density and power density are also

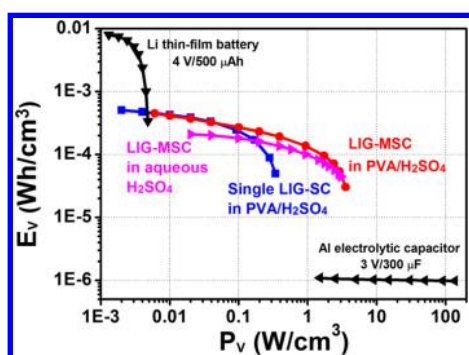


**Figure 6.** Ragone plots of single LIG-SC, LIG-MSC, and commercial energy storage devices. Data of commercial devices were reproduced from refs 10 26, and 27. Data of LIG-MSC in aqueous 1 M  $\text{H}_2\text{SO}_4$  was reproduced from ref 32.

provided in Figure S14 in the Supporting Information to better evaluate their commercial application potential.

## CONCLUSIONS

In summary, we have demonstrated that by using a simple laser induction process, commercially available polyimide substrates can be readily transformed into LIG and then fabricated into flexible and stackable SCs with enhanced capacitive performance. Two different devices, LIG-SCs and LIG-MSCs, were fabricated using PVA/ $\text{H}_2\text{SO}_4$  as a solid polymeric electrolyte and showed outstanding electrochemical performance, cyclability, and excellent flexibility. The simplicity of this LIG device and fabrication process lends itself well to commercial scalability, which could lead to future production of LIG-SC-based devices for the next generation of portable micro-electronics.

## METHODS

### Materials Production and LIG Supercapacitor Fabrication.

Kapton polyimide (PI, Cat. No. 2271K3, thickness: 0.005") was purchased from McMaster-Carr and used as received unless noted otherwise. Laser induction of graphene was conducted with a 10.6  $\mu\text{m}$   $\text{CO}_2$  laser system (Universal X-660 laser cutter platform) at a pulse duration of  $\sim 14 \mu\text{s}$ . All experiments were conducted under ambient conditions using 4.8 W of laser power. Two types of LIG-based SCs were fabricated: single or stacked LIG-SCs and in-plane LIG-MSCs. For single or stacked LIG-SCs, LIG was produced either on one side or both sides of the PI sheet with an active area of 2 cm  $\times$  3 cm, whereas for MSCs, LIG was patterned into interdigitated electrodes with a length of 5 mm, a width of 1 mm, and a spacing of  $\sim 300 \mu\text{m}$  between two neighboring microelectrodes. In both types of structures, Pellico colloidal silver paint (No. 16034, Ted Pella) was applied on the common areas of each electrode for better electrical contacts. The electrodes were then extended with conductive copper tape and connected to an electrochemical workstation. A Kapton PI tape was employed to protect the common areas of the electrodes from electrolyte (see Figure S1 and S2 in the Supporting Information). Polymer electrolyte was made by mixing and stirring 10 mL of DI water, 1 mL of sulfuric acid (98%, Sigma-Aldrich), and 1 g of poly(vinyl alcohol) ( $M_w = 50\,000$ , Aldrich No. 34158-4) at 80  $^\circ\text{C}$  overnight. Solid-state LIG-SCs were fabricated by dropping  $\sim 1 \text{ mL}$  of PVA/ $\text{H}_2\text{SO}_4$  onto a LIG-PI substrate and then sandwiching it with a second LIG-PI substrate. Finally, the device was placed in a desiccator that was connected to house vacuum ( $\sim 10 \text{ mmHg}$ ) to remove excess water overnight. For LIG-MSC devices,  $\sim 0.25 \text{ mL}$  of PVA/ $\text{H}_2\text{SO}_4$  was dropped onto the active LIG area on the PI substrate, followed by placing the device overnight in a desiccator that was connected to house vacuum to remove excess water. For comparison, the MSCs

with aqueous electrolyte were also fabricated by dropping  $\sim 0.2 \text{ mL}$  of 1 M  $\text{H}_2\text{SO}_4$  onto the active LIG on PI sheets.

**Characterization.** SEM images were taken on a FEI Quanta 400 high-resolution field emission SEM. The TEM and HRTEM images were taken using a JEOL 2100F field-emission gun transmission electron microscope. TEM samples were prepared by peeling off LIG from the PI substrate, followed by sonicating them in chloroform, and dropping them onto a lacey carbon copper grid. Raman spectra were recorded on a Renishaw Raman microscope using 514 nm laser with a power of 5 mW. XRD was conducted on a Rigaku D/Max Ultima II with Cu  $K\alpha$  radiation ( $\lambda = 1.54 \text{ \AA}$ ). The surface area of LIG was measured with a Quantachrome Autosorb-3b BET surface analyzer. TGA (Q50, TA Instruments) was carried out at room temperature to 900  $^\circ\text{C}$  at 5  $^\circ\text{C}/\text{min}$  under argon. CV and constant current CC measurements were conducted under ambient conditions using a CHI 608D workstation (USA).

## ASSOCIATED CONTENT

### Supporting Information

Images, spectra, and additional calculation methods. This material is available free of charge via the Internet at <http://pubs.acs.org>.

## AUTHOR INFORMATION

### Corresponding Author

\*E-mail: [tour@rice.edu](mailto:tour@rice.edu).

### Author Contributions

\*Z.P. and J.L. contributed equally to this work.

### Notes

The authors declare no competing financial interest.

## ACKNOWLEDGMENTS

This work was funded by the AFOSR (FA9550-09-1-0581) and the AFOSR MURI (FA9550-12-1-0035).

## REFERENCES

- (1) Liu, C.; Li, F.; Ma, L. P.; Cheng, H. M. Advanced Materials for Energy Storage. *Adv. Mater.* **2010**, *22*, E28–E62.
- (2) Aricò, A. S.; Bruce, P.; Scrosati, B.; Tarascon, J.-M.; Van Schalkwijk, W. Nanostructured Materials for Advanced Energy Conversion and Storage Devices. *Nat. Mater.* **2005**, *4*, 366–377.
- (3) Zhu, Y.; Murali, S.; Stoller, M. D.; Ganesh, K.; Cai, W.; Ferreira, P. J.; Pirkle, A.; Wallace, R. M.; Cychosz, K. A.; Thommes, M. Carbon-Based Supercapacitors Produced by Activation of Graphene. *Science* **2011**, *332*, 1537–1541.
- (4) Zhang, L. L.; Zhao, X. Carbon-Based Materials as Supercapacitor Electrodes. *Chem. Soc. Rev.* **2009**, *38*, 2520–2531.
- (5) Chen, Z.; Ren, W.; Gao, L.; Liu, B.; Pei, S.; Cheng, H.-M. Three-Dimensional Flexible and Conductive Interconnected Graphene Networks Grown by Chemical Vapour Deposition. *Nat. Mater.* **2011**, *10*, 424–428.
- (6) Lin, J.; Zhang, C.; Yan, Z.; Zhu, Y.; Peng, Z.; Hauge, R. H.; Natelson, D.; Tour, J. M. 3-Dimensional Graphene Carbon Nanotube Carpet-Based Microsupercapacitors with High Electrochemical Performance. *Nano Lett.* **2012**, *13*, 72–78.
- (7) Zhang, C.; Peng, Z.; Lin, J.; Zhu, Y.; Ruan, G.; Hwang, C.-C.; Lu, W.; Hauge, R. H.; Tour, J. M. Splitting of a Vertical Multiwalled Carbon Nanotube Carpet to a Graphene Nanoribbon Carpet and Its Use in Supercapacitors. *ACS Nano* **2013**, *7*, 5151–5159.
- (8) Wu, Z. S.; Parvez, K.; Feng, X.; Müllen, K. Graphene-Based in-Plane Micro-Supercapacitors with High Power and Energy Densities. *Nat. Commun.* **2013**, *4*, 2487.
- (9) Chmiola, J.; Largeot, C.; Taberna, P.-L.; Simon, P.; Gogotsi, Y. Monolithic Carbide-Derived Carbon Films for Micro-Supercapacitors. *Science* **2010**, *328*, 480–483.

- (10) Pech, D.; Brunet, M.; Durou, H.; Huang, P.; Mochalin, V.; Gogotsi, Y.; Taberna, P.-L.; Simon, P. Ultrahigh-Power Micrometre-Sized Supercapacitors Based on Onion-Like Carbon. *Nat. Nanotechnol.* **2010**, *5*, 651–654.
- (11) Pech, D.; Brunet, M.; Taberna, P.-L.; Simon, P.; Fabre, N.; Mesnilgrente, F.; Conédéra, V.; Durou, H. Elaboration of a Microstructured Inkjet-Printed Carbon Electrochemical Capacitor. *J. Power Sources* **2010**, *195*, 1266–1269.
- (12) Chen, W.; Beidaghi, M.; Penmatsa, V.; Bechtold, K.; Kumari, L.; Li, W.; Wang, C. Integration of Carbon Nanotubes to C-MEMS for on-Chip Supercapacitors. *IEEE Trans. Nanotechnol.* **2010**, *9*, 734–740.
- (13) Heon, M.; Lofland, S.; Applegate, J.; Nolte, R.; Cortes, E.; Hettinger, J. D.; Taberna, P.-L.; Simon, P.; Huang, P.; Brunet, M. Continuous Carbide-Derived Carbon Films with High Volumetric Capacitance. *Energy Environ. Sci.* **2010**, *4*, 135–138.
- (14) Pandolfo, A.; Hollenkamp, A. Carbon Properties and Their Role in Supercapacitors. *J. Power Sources* **2006**, *157*, 11–27.
- (15) Wang, G.; Zhang, L.; Zhang, J. A Review of Electrode Materials for Electrochemical Supercapacitors. *Chem. Soc. Rev.* **2012**, *41*, 797–828.
- (16) Wang, X.; Liu, B.; Wang, Q.; Song, W.; Hou, X.; Chen, D.; Cheng, Y. B.; Shen, G. Three-Dimensional Hierarchical GeSe<sub>2</sub> Nanostructures for High Performance Flexible All-Solid-State Supercapacitors. *Adv. Mater.* **2013**, *25*, 1479–86.
- (17) Zhang, S.; Peng, C.; Ng, K. C.; Chen, G. Z. Nanocomposites of Manganese Oxides and Carbon Nanotubes for Aqueous Supercapacitor Stacks. *Electrochim. Acta* **2010**, *55*, 7447–7453.
- (18) Denshchikov, K. K.; Izmaylova, M. Y.; Zhuk, A. Z.; Vygodskii, Y. S.; Novikov, V. T.; Gerasimov, A. F. 1-Methyl-3-Butylimidazolium Tetrafluoroborate with Activated Carbon for Electrochemical Double Layer Supercapacitors. *Electrochim. Acta* **2010**, *55*, 7506–7510.
- (19) Ng, K. C.; Zhang, S.; Peng, C.; Chen, G. Z. Individual and Bipolarly Stacked Asymmetrical Aqueous Supercapacitors of CNTs/SnO<sub>2</sub> and CNTs/MnO<sub>2</sub> Nanocomposites. *J. Electrochem. Soc.* **2009**, *156*, A846.
- (20) Beidaghi, M.; Gogotsi, Y. Capacitive Energy Storage in Micro-Scale Devices: Recent Advances in Design and Fabrication of Micro-Supercapacitors. *Energy Environ. Sci.* **2014**, *7*, 867–884.
- (21) Gao, W.; Singh, N.; Song, L.; Liu, Z.; Reddy, A. L. M.; Ci, L.; Vajtai, R.; Zhang, Q.; Wei, B.; Ajayan, P. M. Direct Laser Writing of Micro-Supercapacitors on Hydrated Graphite Oxide Films. *Nat. Nanotechnol.* **2011**, *6*, 496–500.
- (22) Novoselov, K. S.; Geim, A. K.; Morozov, S.; Jiang, D.; Zhang, Y.; Dubonos, S.; Grigorieva, I.; Firsov, A. Electric Field Effect in Atomically Thin Carbon Films. *Science* **2004**, *306*, 666–669.
- (23) Sun, Y.; Wu, Q.; Shi, G. Graphene Based New Energy Materials. *Energy Environ. Sci.* **2011**, *4*, 1113–1132.
- (24) Dai, L. Functionalization of Graphene for Efficient Energy Conversion and Storage. *Acc. Chem. Res.* **2012**, *46*, 31–42.
- (25) Xia, J.; Chen, F.; Li, J.; Tao, N. Measurement of the Quantum Capacitance of Graphene. *Nat. Nanotechnol.* **2009**, *4*, 505–509.
- (26) El-Kady, M. F.; Kaner, R. B. Scalable Fabrication of High-Power Graphene Micro-Supercapacitors for Flexible and on-Chip Energy Storage. *Nat. Commun.* **2013**, *4*, 1475.
- (27) El-Kady, M. F.; Strong, V.; Dubin, S.; Kaner, R. B. Laser Scribing of High-Performance and Flexible Graphene-Based Electrochemical Capacitors. *Science* **2012**, *335*, 1326–1330.
- (28) Tian, H.; Chen, H.-Y.; Ren, T.-L.; Li, C.; Xue, Q.-T.; Mohammad, M. A.; Wu, C.; Yang, Y.; Wong, H.-S. P. Cost-Effective, Transfer-Free, Flexible Resistive Random Access Memory Using Laser-Scribed Reduced Graphene Oxide Patterning Technology. *Nano Lett.* **2014**, *14*, 3214–3119.
- (29) Hummers, W. S., Jr.; Offeman, R. E. Preparation of Graphitic Oxide. *J. Am. Chem. Soc.* **1958**, *80*, 1339–1339.
- (30) Marcano, D. C.; Kosynkin, D. V.; Berlin, J. M.; Sinitskii, A.; Sun, Z.; Slesarev, A.; Alemany, L. B.; Lu, W.; Tour, J. M. Improved Synthesis of Graphene Oxide. *ACS Nano* **2010**, *4*, 4806–4814.
- (31) Dimiev, A. M.; Alemany, L. B.; Tour, J. M. Graphene Oxide. Origin of Acidity, Its Instability in Water, and a New Dynamic Structural Model. *ACS Nano* **2012**, *7*, 576–588.
- (32) Lin, J.; Peng, Z.; Liu, Y.; Ye, R.; Samuel, E. L.; Ruiz-Zepeda, F.; Yacaman, M. J.; Yakobson, B. I.; Tour, J. M. Laser-Induced Porous Graphene Films from Commercial Polymers. *Nat. Commun.* **2014**, *5*, 5714.
- (33) Ferrari, A.; Meyer, J.; Scardaci, V.; Casiraghi, C.; Lazzeri, M.; Mauri, F.; Piscanec, S.; Jiang, D.; Novoselov, K.; Roth, S. Raman Spectrum of Graphene and Graphene Layers. *Phys. Rev. Lett.* **2006**, *97*, 187401.
- (34) Ferrari, A. C. Raman Spectroscopy of Graphene and Graphite: Disorder, Electron–Phonon Coupling, Doping and Nonadiabatic Effects. *Solid State Commun.* **2007**, *143*, 47–57.
- (35) Casiraghi, C.; Hartschuh, A.; Qian, H.; Piscanec, S.; Georgi, C.; Fasoli, A.; Novoselov, K.; Basko, D.; Ferrari, A. Raman Spectroscopy of Graphene Edges. *Nano Lett.* **2009**, *9*, 1433–1441.
- (36) Gupta, A. K.; Russin, T. J.; Gutiérrez, H. R.; Eklund, P. C. Probing Graphene Edges Via Raman Scattering. *ACS Nano* **2008**, *3*, 45–52.